The effect of seismic radiation patterns on the interpretation of SKS splitting: evidence from Phase 2 of the WA Array

M. Gauntlett[1], C. M. Eakin[1], M. S. Miller[1]

[1]Research School of Earth Sciences, Australian National University, Acton, ACT, 0200

This is a non-peer-reviewed preprint submitted to EarthArXiv. The original manuscript has been submitted to Seismological Research letters.

The effect of seismic radiation patterns on the interpretation of SKS splitting: evidence from Phase 2 of the WA Array

Miriam Gauntlett*[1], Caroline M. Eakin[1], and Meghan S. Miller[1]

Abstract

Coherent anisotropic fabrics trending E–W to NE–SW across Western Australia have been revealed by shear-wave splitting of the SKS and PKS (XKS) phases across the WA Array. This large temporary array of 130 stations with 40 km spacing shows that this seismic anisotropy is pervasive; yet individual stations, including permanent ones, produce relatively few results. We investigate the effect of focal mechanism orientation on the XKS energy radiated from an event, and find that XKS energy is at a minimum when the raypath is aligned with an event nodal plane. This coincidence occurs often for events occurring in South America or the Aleutians, two of the main source regions for XKS events that are recorded in Western Australia. We determine that the reduction in XKS energy when the raypath is close to the nodal plane is significant enough to affect our ability to make XKS measurements. We propose that this is why Western Australia has a historic lack of XKS measurements even in the presence of coherent seismic anisotropy. We also suggest that a lack of XKS splitting is not unequivocal evidence for apparent isotropy or weak anisotropy. Focal mechanism orientation is an important consideration when interpreting the productivity of shear-wave splitting studies.

Cite this article as Gauntlett M., Eakin C. M., and Miller M. S. (2022). The effect of seismic radiation patterns on the interpretation of SKS splitting: evidence from Phase 2 of the WA Array, *Seismol. Res. Lett.* **XX**, 1–19, doi: 00.0000/000000000.

Supplemental Material

1. Research School of Earth Sciences, Australian National University, Acton, ACT, 0200

*Corresponding author: miriam.gauntlett@anu.edu.au

Introduction

Seismic anisotropy is the directional dependence of shear wave velocity, primarily arising due to viscous flow and deformation within the upper mantle (Nicolas and Christensen, 1987; Kendall and Silver, 1996). The upper mantle is dominated by anisotropic olivine crystals, which respond to deformation by adopting a preferred crystal orientation (Nicolas and Christensen, 1987). Measurement of this Earth property can therefore provide information on active dynamic processes currently deforming the asthenosphere; or past deformation episodes such as orogenies that are 'fossilised' into the lithosphere (Long and Becker, 2010).

Western Australia (WA) is one of the most ancient continental regions in the world, having formed and stabilised over 2 billion years ago in the Archean era. Beneath WA lies very thick continental lithosphere (> 250 km at its thickest point) that has undergone significant deformation since its assembly. Australia is also one of the fastest-moving continents, with an absolute plate motion speed of ~8cm/yr directed approximately NNE in the fixed hotspot reference frame (Gripp and Gordon, 2002). These features have prompted questions about the nature of seismic anisotropy beneath WA: is it dominated by fossilized lithospheric fabric, or does the current mantle flow field control the pattern of anisotropy?

One of the most common methods for investigating seismic anisotropy of the upper mantle is shear-wave splitting of the SKS, PKS and SKKS phases (Savage, 1999). These phases pass through the core as P-waves, and thus are polarised in the direction of travel when they emerge from the core-mantle boundary as S-waves, with all energy polarised on the radial component. When these shear waves meet an anisotropic layer within the Earth, they split into two 'quasi' shear waves, polarised approximately orthogonal to each other, separated by a time delay. For XKS phases, the splitting process produces energy on the transverse component, generating elliptical particle motion. The fast polarisation orientation (ϕ) and the time delay (δt) between the two waves characterise the anisotropic medium the waves passed through. Calculating these splitting parameters across a seismic network can therefore reveal past and present deformational processes in the mantle such as plate-motion driven shear flow in the asthenosphere (e.g., Eakin et al., 2023), or map ancient tectonic boundaries within continental lithosphere (Fouch and Rondenay, 2006; Eakin et al., 2021).

Shear-wave splitting studies in WA have heretofore been limited by the station coverage in this part of the continent: permanent stations are spaced several hundred kilometres apart, whereas temporary arrays often have short deployment periods (e.g., Geoscience Australia, 2021; Balfour et al., 2014; Tkalčić et al., 2013). The ongoing WA Array project addresses this issue, aiming to cover the entire state of WA with seismic instruments over 10 years and 9 phases of deployment (Murdie et al., 2024). Each phase will involve around ~130 seismometers, with a close station spacing of ~40 km.

Before the WA Array deployment, early analyses of seismic anisotropy beneath permanent stations in WA reported very few or no shear-wave splitting measurements, suggesting that the region may be apparently isotropic (Özalaybey and Chen, 1999; Heintz and Kennett, 2006). Later studies, utilising more years of data from the permanent network, had more success at producing shear-wave splitting results in WA (Chen et al., 2021; Birkey and Ford, 2023; Ba et al., 2023), although seismic anisotropy was still proposed to be 'weak' at two permanent stations in WA (Chen et al., 2021). A shear-wave splitting analysis of Phase 1 of the WA Array (~130 temporary stations deployed from November 2022 to December 2023) and the SWAN network (27 temporary stations deployed from September 2020 to September 2023; Miller et al., 2023), the largest temporary networks ever deployed in WA, revealed large-scale coherent anisotropic fabrics underlying the region, directed primarily E–W to NE–SW (Gauntlett et al., 2025). However, the number of measurements produced by all of these studies was still far lower than expected in comparison to other regions: approximately one or two per year at each station.

The presence of coherent seismic anisotropy in WA but a limited number of shear-wave splitting measurements is puzzling. In this contribution, we investigate the effect of the radiation pattern from available earthquakes on the productivity of shear-wave splitting studies and consider this in the context of the XKS results from Phase 2 of the WA Array project.

Phase 2 Analysis

As part of the WA Array project, we carried out shear-wave splitting analysis for SKS and PKS phases on 130 temporary seismic stations deployed across the southwest of the state from March 2024 – March 2025 (Phase 2 of the project). We search the ISC earthquake catalogue for teleseismic earthquakes with magnitude $M_b > 5.75$, occurring in epicentral distance ranges 87–130° and 130–150° from the study region. These ranges distinctly capture the SKS and PKS (XKS) phases, respectively. We apply a bandpass filter to these data, using a frequency range of 0.04–0.125 Hz to produce clear XKS signals.

We use the SplitLab software to calculate the shear-wave splitting parameters (Wüstefeld et al., 2008), and report the result produced by the rotation correlation (RC) method (Bowman and Ando, 1987). This method produced the most stable results compared to the other two methods available in SplitLab.

Figure 1 shows the full results obtained by our analysis, with Phase 2 stations supplemented by 8 permanent stations from the AU and S1 networks (Geoscience Australia, 2021; Balfour et al., 2014). We also use data from 14 temporary stations from the OA network (operational between November 2022 – March 2025; Gorbatov et al., 2020), and 21 stations from the 1K network (operational between November 2013 – September 2015; Tkalčić et al., 2013). The Phase 2 data were subject to rigorous quality assurance and quality control metrics, providing a high-quality and reliable dataset (Ebrahimi, 2026).

The fast direction of seismic anisotropy is directed predominantly E–W to NE–SW across the Phase 2 stations, consistent with previous findings from Phase 1 (active from November 2022 to December 2023; navy bars in Figure 1) and SWAN (active from September 2020 to September 2023; dark red bars in Figure 1). We have previously interpreted this anisotropic fabric as reflecting ancient lithospheric deformation, likely related to the formation of the continent (Gauntlett et al., 2025). For a preliminary discussion of the Phase 2 results, see Gauntlett and Eakin (2026). In the following, we focus on analysing the details of the shear-wave splitting productivity for these stations.

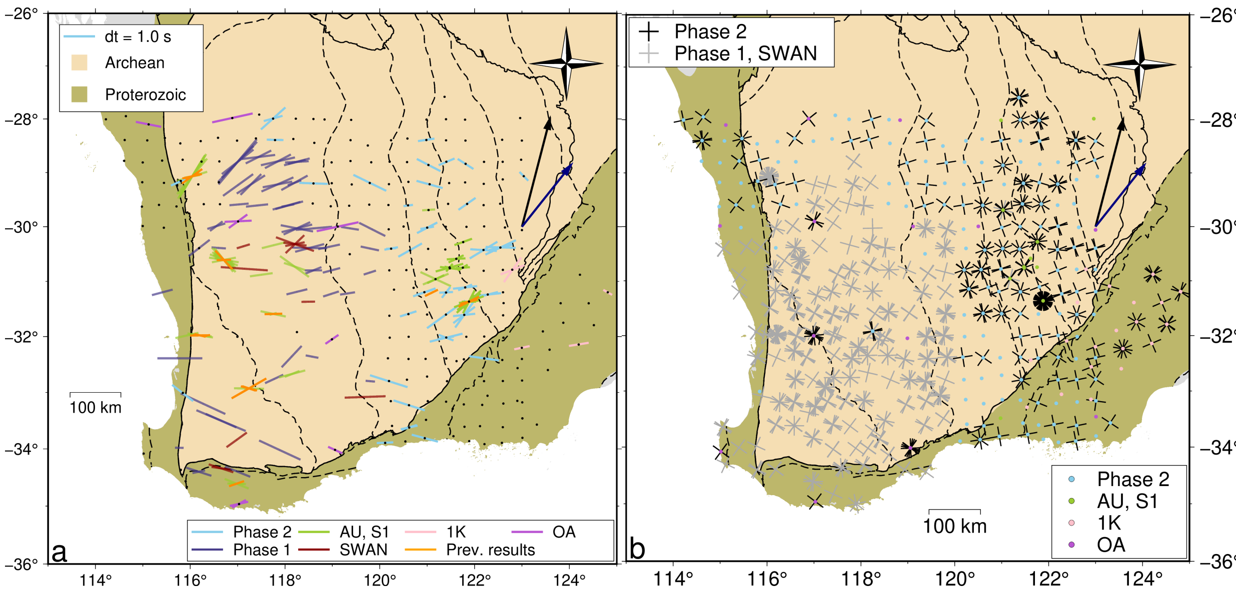

Figure 1. Map of XKS splitting parameters. a) Each measurement is plotted as a bar oriented parallel to the fast polarisation direction, ϕ, with length scaled to δt. WA Array Phase 2 results are plotted in blue, supplemented with permanent stations from the AU and S1 networks in the Phase 2 area (green; Geoscience Australia, 2021; Balfour et al., 2014), 1K stations (pink; Tkalčić et al., 2013) and OA stations (purple; Gorbatov et al., 2020). Black dots represent all stations analysed in the Phase 2 study area. WA Array Phase 1 results are plotted in dark blue, SWAN results are plotted in dark red, supplemented with AU and S1 permanent stations in the Phase 1 area (green). Previous XKS estimates within the region are plotted in orange (Vinnik et al., 1992; Heintz and Kennett, 2005; Chen et al., 2021; Ba et al., 2023; Birkey and Ford, 2023). The black arrow shows the apparent plate motion from the HS3-NUVEL 1A model (Gripp and Gordon, 2002) and the navy arrow shows the apparent plate motion from the NNR-MORVEL56 model (Argus et al., 2011). Dashed black lines are the major crustal boundaries of Western Australia, with the Yilgarn craton outlined in solid black (Martin et al., 2021). b) Map of the XKS null results calculated across the Phase 1 (grey) and Phase 2 (black) study areas, plotted as crosses oriented to the backazimuth of the event. Phase 2 area stations are colour-coded as in a).

Alt text: Map of XKS splitting parameters in Western Australia. Left panel shows split results plotted as a bar oriented parallel to the fast polarisation direction and length scaled to δt. Results are colour-coded by network. Right panel shows null results plotted as crosses oriented to the backazimuth of the event.

Phase 2 results

Overall, the Phase 2 stations returned only 48 splitting measurements from 130 stations, less than 1 per station (blue bars in Figure 1a), and 146 null measurements (black crosses in Figure 1b). Only 11 separate events produced results (either a split or a null) across the network (Figure 2a, Table 1) out of ~50–60 available earthquakes.

Results are classified as 'nulls' when there appears to be no splitting experienced by the shear wave; that is, the initial particle motion is linear rather than elliptical and there is no visible energy on the transverse component. These nulls can occur when the initial polarisation of the shear wave (equal to its backazimuth for XKS phases) matches the fast or slow polarisation orientation of the anisotropic medium.

We propose that the predominance of nulls over splits (3:1 ratio) is due to the prevalence of the available events used in the study being aligned close to the backazimuth of the fast (or slow) direction of the anisotropy (see Figure 4 in Gauntlett and Eakin, 2026). The same conclusion was reached for our Phase 1 analysis, where nulls made up approximately 80% of the total results (see Figure 4 in Gauntlett et al., 2025). Contributing factors to this phenomenon include the limited distance

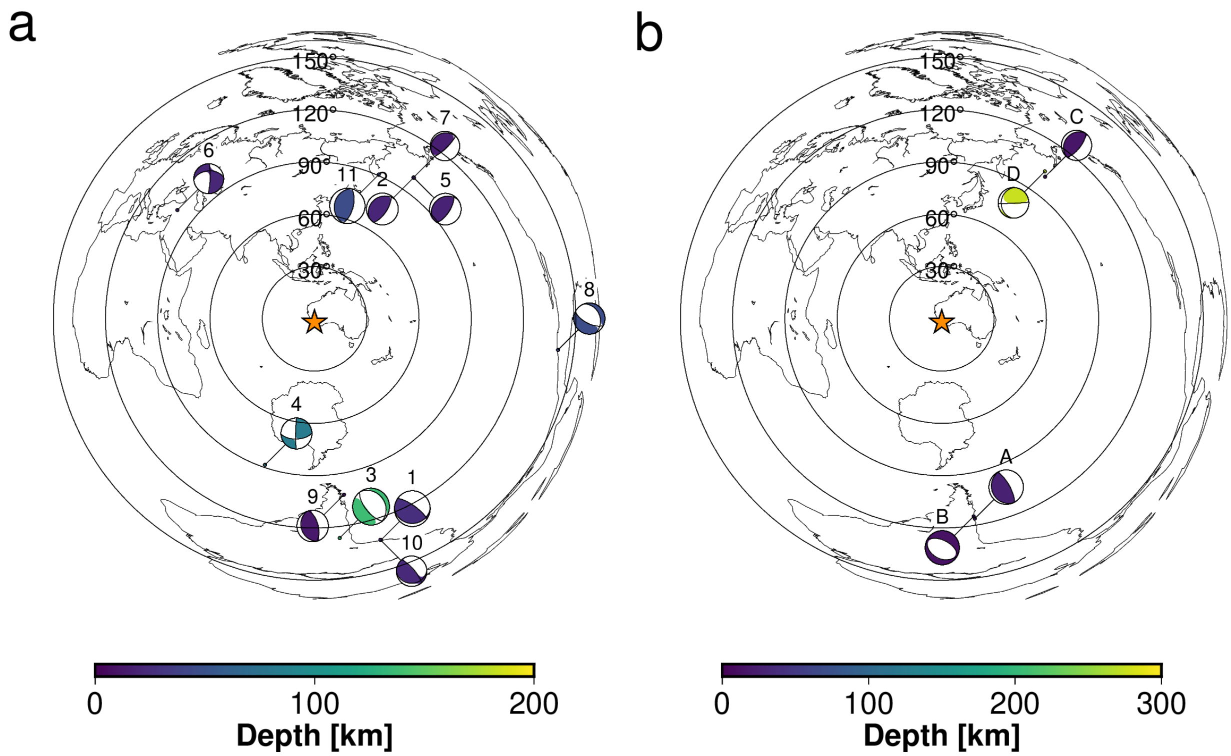

Figure 2. Focal mechanisms obtained from the Global Centroid Moment Tensor catalogue (Dziewonski et al., 1981; Ekström et al., 2012), coloured by depth. a) The eleven events that produced results for the XKS splitting analysis of Phase 2 stations of the WA Array. Table 1 lists the events. b) Events A–D, as discussed in Figures 7 and 8 and associated text.

Alt text: Focal mechanisms obtained from the Global Centroid Moment Tensor catalogue, coloured by depth. Left panel shows events that produced results for the XKS splitting analysis of the WA Array. Right panel shows events A–D as discussed later in the text.

range for SKS and PKS phases (87°– 130°and 130°– 150°, respectively) and the limited time deployment of each phase of the WA Array (approximately one year), reducing the available backazimuthal coverage for the stations.

Permanent stations

The lack of shear-wave splitting measurements at WA Array stations cannot solely be attributed to their short deployment time. Looking at permanent stations in WA, a similar pattern emerges across previous studies (Table 2), with very few split results measured relative to the station deployment time. Most studies report less than 1 split per year of data analysed.

As an example, station KMBL has been running for 21 years. Our analysis produces 23 split results out of 1,154 available earthquakes, a success rate of only 2% (Figure 3). Studies using similar methodologies on permanent stations from other regions tend to produce split results at a rate of 10–15% (e.g., Eakin and Long, 2013; Eakin et al., 2010; Liu et al., 2014). The discrepancy for WA can partially be explained by the bias towards nulls due to the inferred anisotropic geometry and the backazimuthal coverage of events. However, the number of null results is also relatively for station KMBL, with only 60 null results, equating to a success rate of only 5%.

TABLE 1.
Events producing an XKS result (split or null) for Phase 2 stations.

Event	Date	Lat (°)	Lon (°)	No. of results
1	28-Jun-2024	-15.89	-74.75	51
2	8-Dec-2024	51.07	-177.31	48
3	19-Jul-2024	-23.14	-67.72	41
4	01-Jan-2025	-56.46	-26.47	16
5	09-Dec-2024	51.02	-177.17	14
6	16-Oct-2024	38.31	38.85	8
7	10-Dec-2024	51.16	-177.28	5
8	12-Jan-2025	18.60	-103.29	5
9	08-Nov-2024	-75.63	-46.72	4
10	29-Jun-2024	-16.08	-74.68	1
11	17-Aug-2024	52.79	160.27	1

TABLE 2.
Shear-wave splitting results (splits only) from AU network seismic stations.

Station	Years analysed	Study	SKS Split Results	PKS Split Results	SKKS Split Results	Total
MORW	9	Chen et al. (2021)	3	3	13	20
	15	Ba et al. (2023)	6	–	–	6
	N/A	Birkey and Ford (2023)	10	–	1	11
	20	Gauntlett et al. (2025)	9	–	–	9
MUN	9	Chen et al. (2021)	5	7	7	19
	17	Ba et al. (2023)	1	–	–	1
	N/A	Birkey and Ford (2023)	10	–	–	10
	22	Gauntlett et al. (2025)	2	–	–	2
KMBL	9	Chen et al. (2021)	5	3	6	15
	18	Ba et al. (2023)	10	2	–	12
	N/A	Birkey and Ford (2023)	13	–	3	16
	21	Gauntlett et al. (2025)	21	2	–	23

The low rate of return from shear-wave splitting studies in WA therefore appears to be independent of the length of deployment of the stations analysed and is not compensated by an increased number of nulls. We therefore need to investigate an alternative explanation for this low productivity (i.e., low shear-wave splitting success rate). In particular, how might the radiation of seismic energy from different source focal mechanisms affect XKS measurements?

Focal mechanisms

When plotting the available events for SKS splitting in WA, we noted that one of the main sources of events was the South America subduction zone, which has plentiful events but produces few results. These earthquakes have predominantly normal or reverse thrusting mechanisms, with the strike of the fault plane usually aligned N–S. The great circle paths connecting

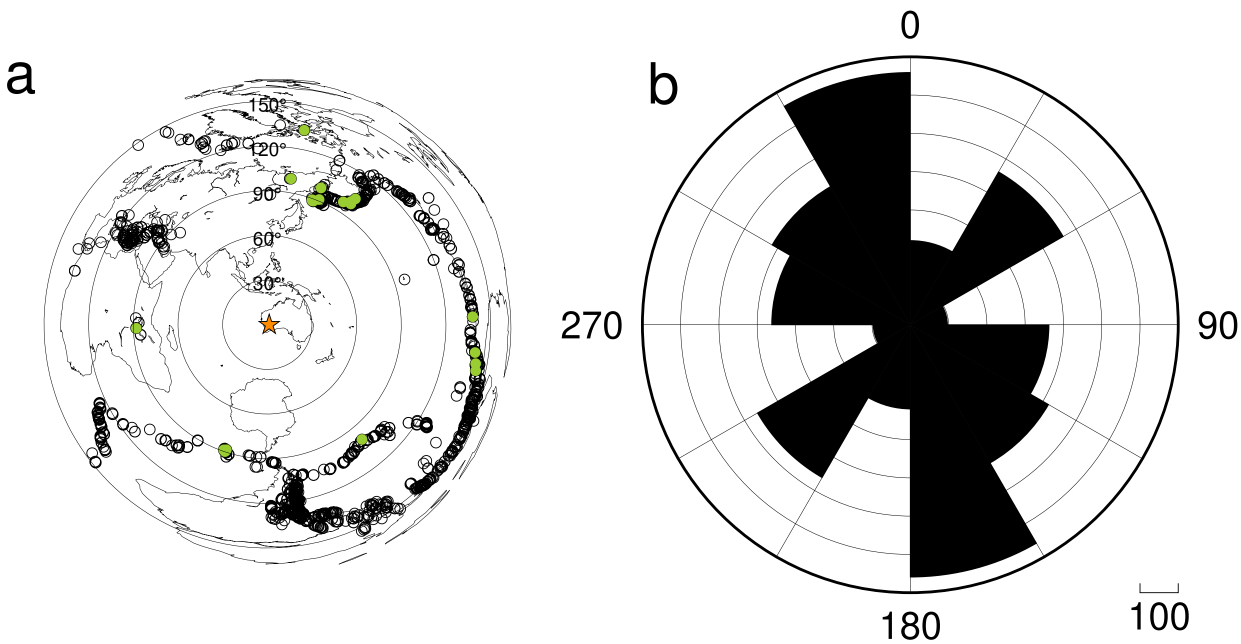

Figure 3. a) Map of available events for XKS splitting for permanent station KMBL (AU network, orange star) between 2000 and 2025 (events in the distance range 90° to 130° for SKS and 130° to 150° for PKS). Events that produced a split result are coloured in green. b) Polar histogram for all available events.

Alt text: Left panel shows the global distribution of all available events for XKS splitting for permanent station KMBL. Events producing a split result are coloured in green. Right panel shows a polar histogram for all available events.

these events to WA head south, with the azimuth of the raypath often similar to the orientation of the nodal planes (Figure 4). Such a coincidence prompts the further investigation of the directional effect of the source radiation pattern.

The focal mechanism of an earthquake describes the pattern of deformation induced by a fault slip. The geometry of and motion along the fault determines the emanation of seismic energy from the earthquake (i.e., the radiation pattern). The amount of seismic energy radiated varies with ray azimuth, as well as take-off angle (Boore and Boatwright, 1984; Aki and Richards, 2002). For P-waves, the radiation pattern has two nodal planes where displacement will be zero. One of these nodal planes corresponds to the fault plane that ruptured during the earthquake, and the other is the auxiliary plane, orthogonal to the fault plane.

The typical illustration of a focal mechanism is a 'beachball', derived from these P-wave first motions. Figure 5 shows these beachballs for the standard double-couple mechanisms: a thrust (reverse) fault (a), a strike-slip fault (b) and a normal fault (c). Compressional regions are shaded and dilatational regions are left blank. The three principal axes are marked: the tension (T) axis indicating maximum compressional motion, the pressure (P) axis indicating maximum dilatational motion and the null (N) axis indicating the intersection of the two focal planes.

For S-waves, the radiation pattern is a combination of the horizontal and vertical S-wave components (SH and SV, respectively). In Figure 5d–i, we plot the expected radiation pattern for the SH and SV components for the three double-couple mechanisms (Boore and Boatwright, 1984; Aki and Richards, 2002). The SV radiation pattern for a thrust fault (Figure 5d) is 'two-lobed', with maxima at 90° and 270° and minima at 0° and 180°. The same is true for a normal fault (Figure 5f) but

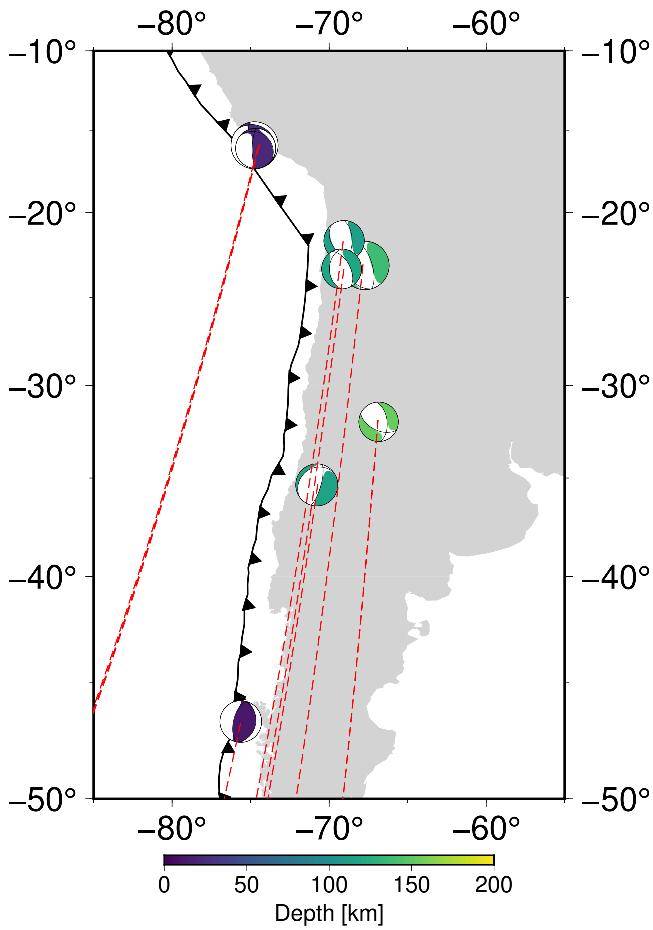

Figure 4. Map of available events for SKS splitting for Phase 2 WA Array stations in South America (i.e., events in the epicentral distance range 87° to 130°). Red dashed lines are the great circle paths from these events to WA. The focal mechanisms are obtained from the Global Centroid Moment Tensor catalogue (Dziewonski et al., 1981; Ekström et al., 2012), coloured by depth. Thick black line is the plate boundary between the South America and Nazca/Antarctica plates, with the subduction down-dip direction indicated by black triangles (Bird, 2003).

Alt text: Map of available events SKS splitting for Phase 2 WA Array stations in South America (i.e., events in the epicentral distance range 87° to 130°), connected by red dashed lines indicating the raypaths from these events to WA.

the amplitude sign is reversed. The SV pattern for a strike-slip fault (Figure 5e) is 'four-lobed', with minima at 0°, 90°, 180° and 270°. Maxima are seen at 45°, 135°, 225° and 315°.

SH radiation patterns for all three focal mechanisms are four-lobed. Figure 5g and 5i for thrust and normal faults respectively show minima at 0°, 90°, 180° and 270° and maxima at 45°, 135°, 225° and 315°, differing only in the sign of the amplitude. Figure 5h shows the SH strike-slip radiation pattern, which has maxima at 0°, 90°, 180° and 270° and minima at 45°, 135°, 225°.

However, it is important to remember that the radiation pattern of seismic energy is three-dimensional. To assist visualisation, we have plotted interactive radiation patterns for teleseismic SV and SH radiation based on the equations of Boore and Boatwright (1984) for simple strike-slip and dip-slip faults (see Supplementary Figures 1–3).

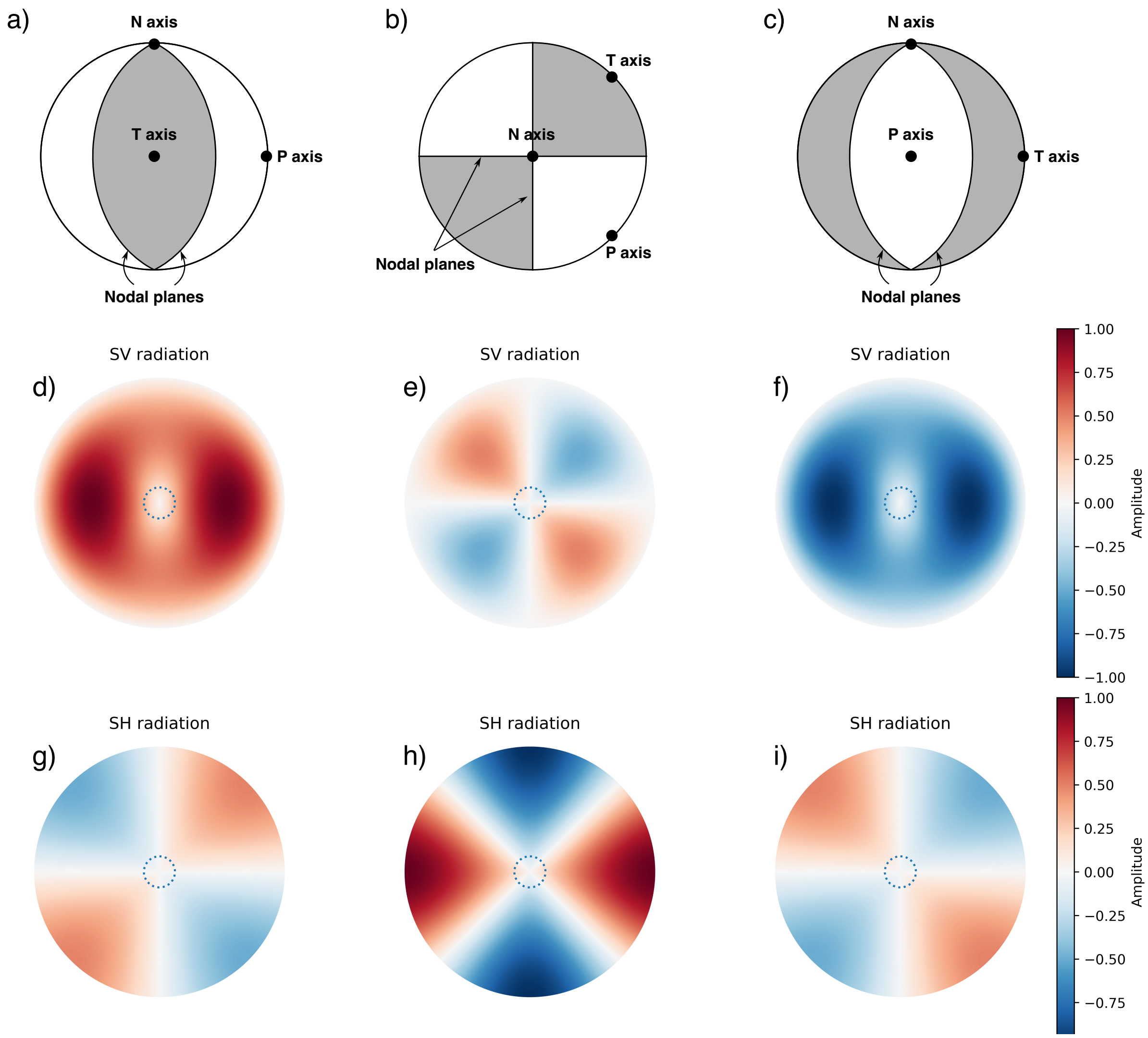

Figure 5. a–c) Typical focal mechanism depictions of P-wave first motions for standard double-couple mechanisms: a dip-slip thrust (or reverse) fault (a), a strike-slip fault (b) and a dip-slip normal fault (c). Compressional quadrants are shaded in grey, while dilatational quadrants are left blank. The null (N) axis is the intersection of the nodal planes. The tension (T) axis marks maximum compressional motion. The pressure (P) axis indicates maximum dilatational motion. d–i) SV and SH radiation patterns for the lower half of the focal sphere, corresponding to the focal mechanisms above. The takeoff angle for a typical SKS phase ($\sim 10°$) is indicated by the dotted line.

Alt text. Top row: P-wave first motions focal mechanisms for a dip-slip thrust fault, a strike-slip fault and a normal fault. Middle row: SV radiation patterns for the lower half of the focal sphere, corresponding to the focal mechanisms above. Bottom row: SH radiation patterns for the lower half of the focal sphere, corresponding to the focal mechanisms above.

To look at potential effects of radiation pattern variation on SKS energy, we calculate synthetics using Instaseis, which computes broadband seismograms from Green's function databases generated with AxiSEM (van Driel et al., 2015; Nissen-Meyer et al., 2014). We also make use of Syngine, which extracts Instaseis databases hosted by the EarthScope DMC (Krischer et al., 2017). We are therefore able to quickly and easily produce synthetic seismograms for the standard double-couple focal mechanisms: a thrust fault and a strike-slip fault, illustrated in Figure 5. Although real focal mechanisms will be more complex than these idealised cases, these provide simple end-member cases for what to expect.

In these simple examples, the thrust fault has strike 0°, dip 45° and rake 90°, while the strike-slip fault has strike 0°, dip 90° and rake 180°. In Figure 6 we plot the amplitude of the radial component of the SKS phase after varying the source-station azimuth between 0° and 360°, while the epicentral distance is kept fixed at 95°. The resulting plots show that the radial amplitude of the SKS phase from the thrust fault (top, purple) is a minimum at azimuths of 0° and 180°, while the strike-slip fault (bottom, orange) shows minima at 0°, 90°, 180° and 270°. The minimum radial energy for the strike-slip fault is 0, whereas the radial amplitude does not go to 0 for the thrust fault.

These amplitude variations follow the SV radiation patterns from Figure 5d and e and Supplementary Figures 1 and 2 rather than the SH patterns. The thrust mechanism shows a two-lobed pattern with 180° periodicity (Figure 5d) and the strike-slip mechanism shows a four-lobed pattern with 90° periodicity (Figure 5e). This is because SKS phases travel through the liquid outer core. When an S-wave impinges on the core-mantle boundary, only the energy polarised in the vertical plane of incidence (SV) can convert into a P-wave. These amplitude calculations from synthetic seismograms (Figure 6) and the radiation patterns plotted in Figure 5 demonstrate that the SKS energy at a station will be a minimum for ray azimuths parallel to the strike of the nodal planes for pure dip-slip or pure strike-slip faults.

Our investigation of amplitude variations indicates that a coincidence between the fault plane strike and the raypath azimuth, as is common for our events in South America (Figure 4), will likely substantially reduce the amplitude of the seismic energy associated with the SKS phase. We therefore explore the measurable effect this has on the ability to make a shear-wave splitting measurement.

Observed Effect of Focal Mechanism Orientation

Real earthquakes are often a combination of strike-slip and dip-slip mechanisms; such oblique-slip radiation patterns can be more complex. Nevertheless, we assume that the SV radiation emanated from an earthquake will be minimised approximately parallel to the strike of the nodal planes if the earthquake is predominantly strike-slip or dip-slip. We therefore hypothesise that if the strike of the fault (or the auxiliary) plane is closely coincident with the great circle path, then the resultant XKS energy will be diminished sufficiently such that making a good quality shear wave splitting measurement is difficult or impossible.

We illustrate this in Figure 7, using two earthquakes from South America that are in the appropriate distance range for the SKS phase (events A and B in Figure 2b). Event A is 108.5° from station EIDS, a station from the AU permanent network in Queensland and 117° from station MORW, a station from the AU permanent network in WA. Event B is 107° from station EIDS and 115° from station MORW. Event A has a typical focal mechanism for the subduction zone: a thrust fault with a strike of 179°. Event B is a normal fault with a strike of 144°, which is atypical given the subduction zone geometry (see black line with triangles in Figure 7). For event A, SKS energy is clearly visible on the radial (Q) component at station EIDS. In this case the great circle path is at a clear angle to the orientation of the nodal planes. By contrast, station MORW shows very

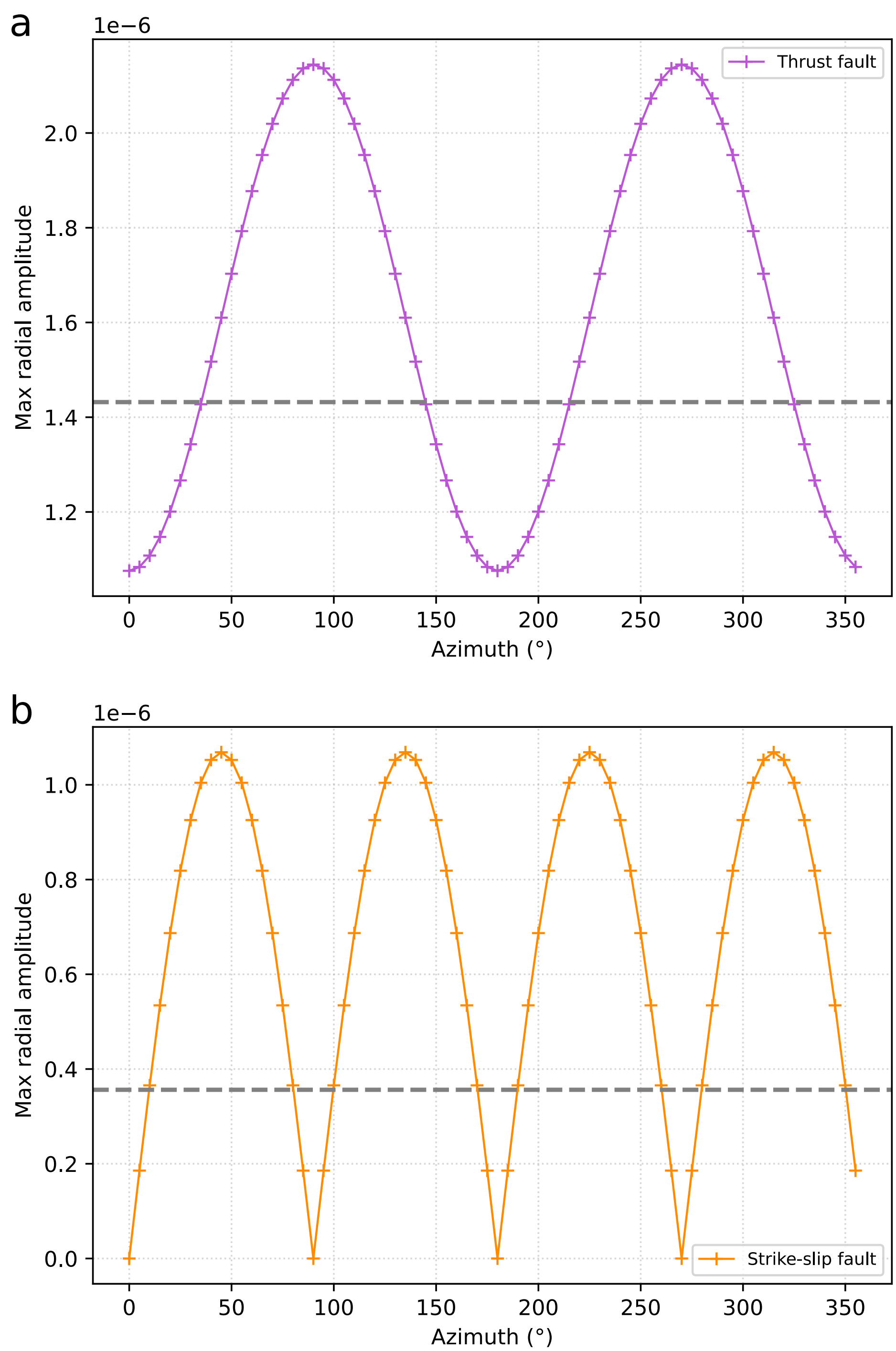

Figure 6. Amplitude variations for the radial component of the SKS phase from a thrust fault (a) and a strike-slip fault (b) as source-station azimuth changes, calculated using synthetics based on an isotropic Earth model (van Driel et al., 2015; Krischer et al., 2017; Nissen-Meyer et al., 2014). Dashed grey lines mark 33% of the peak-to-peak amplitude of the curves. The focal mechanism of the thrust fault is the same as Figure 5a, and the focal mechanism of the strike-slip fault is the same as Figure 5b.

Alt text: Graph of amplitude variations for the radial component of the SKS phase from a thrust fault (top) and a strike-slip fault (bottom) as source-station azimuth changes, calculated using synthetics based on an isotropic Earth model.

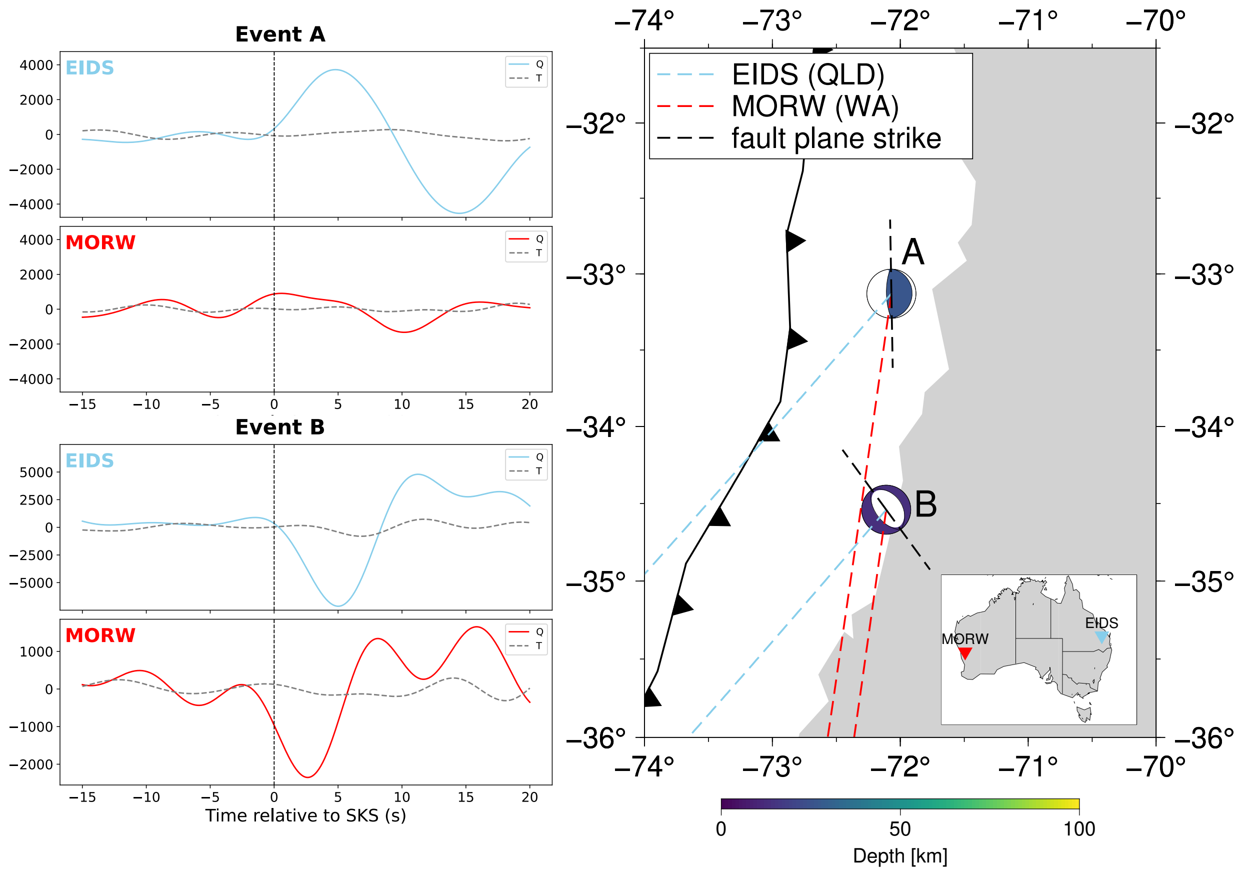

Figure 7. Left panels: Comparison of the SKS energy recorded by two events in South America at two AU network stations, EIDS in Queensland and MORW in WA. Radial (Q) components are plotted in solid colour (red for MORW and blue for EIDS), while transverse (T) components are plotted in dashed grey. Vertical dashed lines indicate the predicted SKS arrival time from Earth model iasp91. Event A shows measurable SKS energy at EIDS but not at MORW, while event B shows measurable SKS energy at both. Right panel: The focal mechanisms are obtained from the Global Centroid Moment Tensor catalogue (Dziewonski et al., 1981; Ekström et al., 2012), coloured by depth. Dashed black lines plot the fault plane strike. Coloured dashed lines show the ray azimuth from each event to station EIDS (blue) and to station MORW (red). Inset shows the location of stations EIDS and MORW on the Australian continent. Thick black line is the plate boundary between the South American and Nazca plates, with the subduction down-dip direction indicated by black triangles (Bird, 2003).

Alt text: Left panel: Comparison of the SKS energy recorded by two events in South America at two AU network stations, EIDS in Queensland and MORW in WA. Right panel: the two events plotted on a map along with the fault plane strikes and the great circle paths connecting them to the stations.

little SKS energy, with a great circle path that is separated by less than 5° from the strike of the fault plane. For event B, both EIDS and MORW have great circle paths oriented at large angles (> 44°) to the strike of the nodal planes. In this case, SKS energy is visible at both stations.

Another principal source of earthquakes for SKS splitting in WA is the subduction zone beneath the Aleutians (Figures 2 and 3). Figure 8 shows the focal mechanisms for two earthquakes from the Aleutians (events C and D in Figure 2b) and their corresponding SKS energy measured at a station in New South Wales (RIV) and a station in WA (KMBL). Event C is 90.5° from station RIV and 100° from station KMBL. Event D is 93° from station RIV and 102° from station KMBL. Event C has a thrust fault mechanism with a strike of 67°, aligned with the trench and typical for the subduction zone, while event D

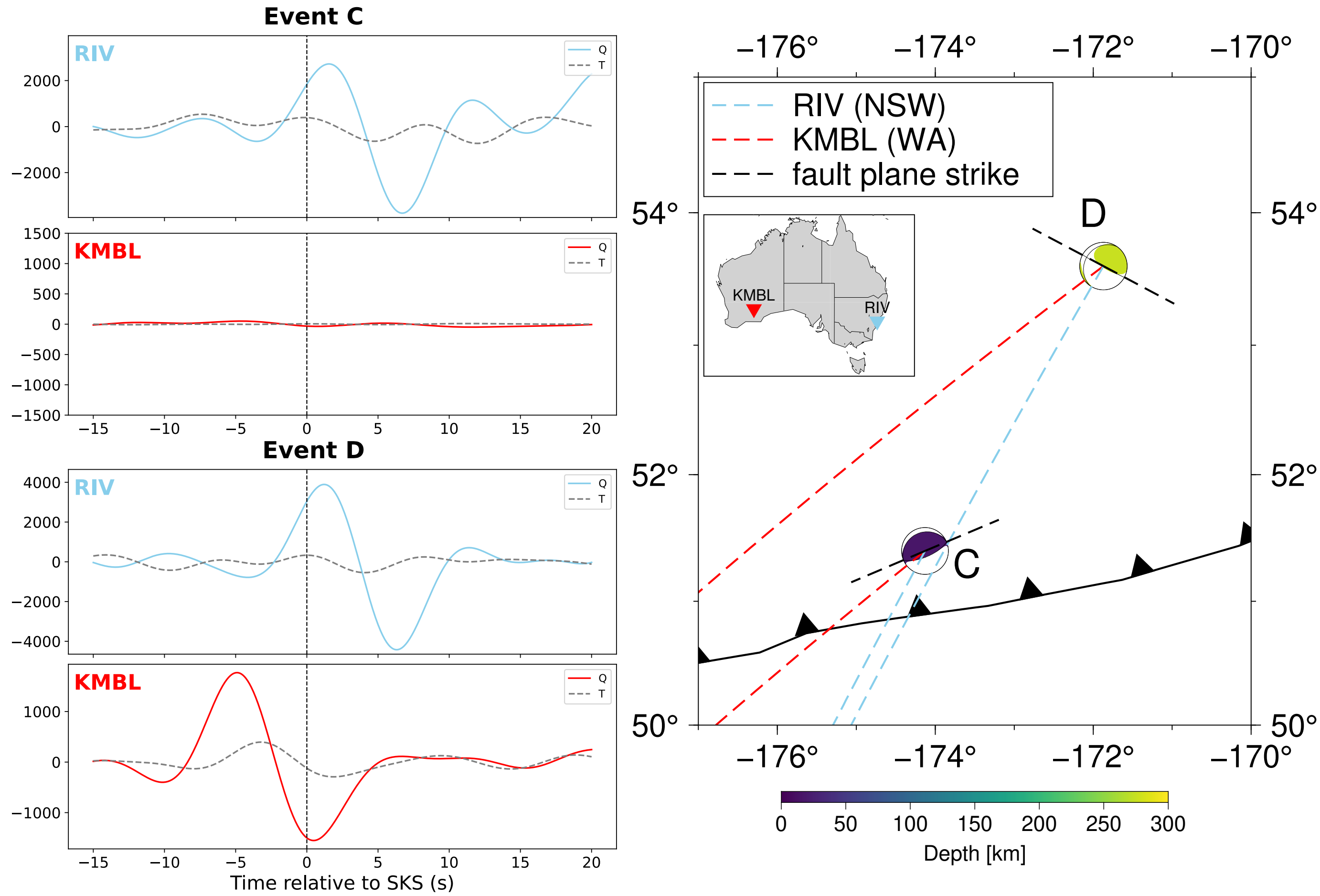

Figure 8. Left panels: Comparison of the SKS energy recorded by two events in the Aleutians at two AU network stations, RIV in New South Wales and KMBL in WA. Radial (Q) components are plotted in solid colour (red for KMBL and blue for RIV), while transverse (T) components are plotted in dashed grey. Vertical dashed lines indicate the predicted SKS arrival time from Earth model iasp91. Event C shows measurable SKS energy at RIV but not at KMBL, while event D shows measurable SKS energy at both. Right panel: The focal mechanisms are obtained from the Global Centroid Moment Tensor catalogue (Dziewonski et al., 1981; Ekström et al., 2012), coloured by depth. Dashed black lines plot the fault plane strike. Coloured dashed lines show the ray azimuth from each event to station RIV (blue) and to station KMBL (red). Inset shows the location of stations KMBL and RIV on the Australian continent. Thick black line is the plate boundary between the North American and Pacific plates, with the subduction down-dip direction indicated by black triangles (Bird, 2003).

Alt text: Left panel: Comparison of the SKS energy recorded by two events in South America at two AU network stations, RIV in New South Wales and KMBL in WA. Right panel: the two events plotted on a map along with the fault plane strikes and the great circle paths connecting them to the stations.

is atypical with a more complex mechanism that is partially thrust and partially strike-slip. The fault plane of event D has a strike of 118°. Station RIV, with great circle paths oriented at large angles to the nodal planes, shows clear SKS energy on the radial (Q) component for both event C and D. However, station KMBL only shows visible SKS energy for the atypical event D, where its great circle path is oriented at a far greater angle to the nodal planes than for event C.

Synthetic Tests

To further corroborate these observations, we calculate synthetic seismograms for an event with the same focal mechanism as event A observed at the same epicentral distance of stations EIDS and MORW. We vary the azimuth of the event to observe

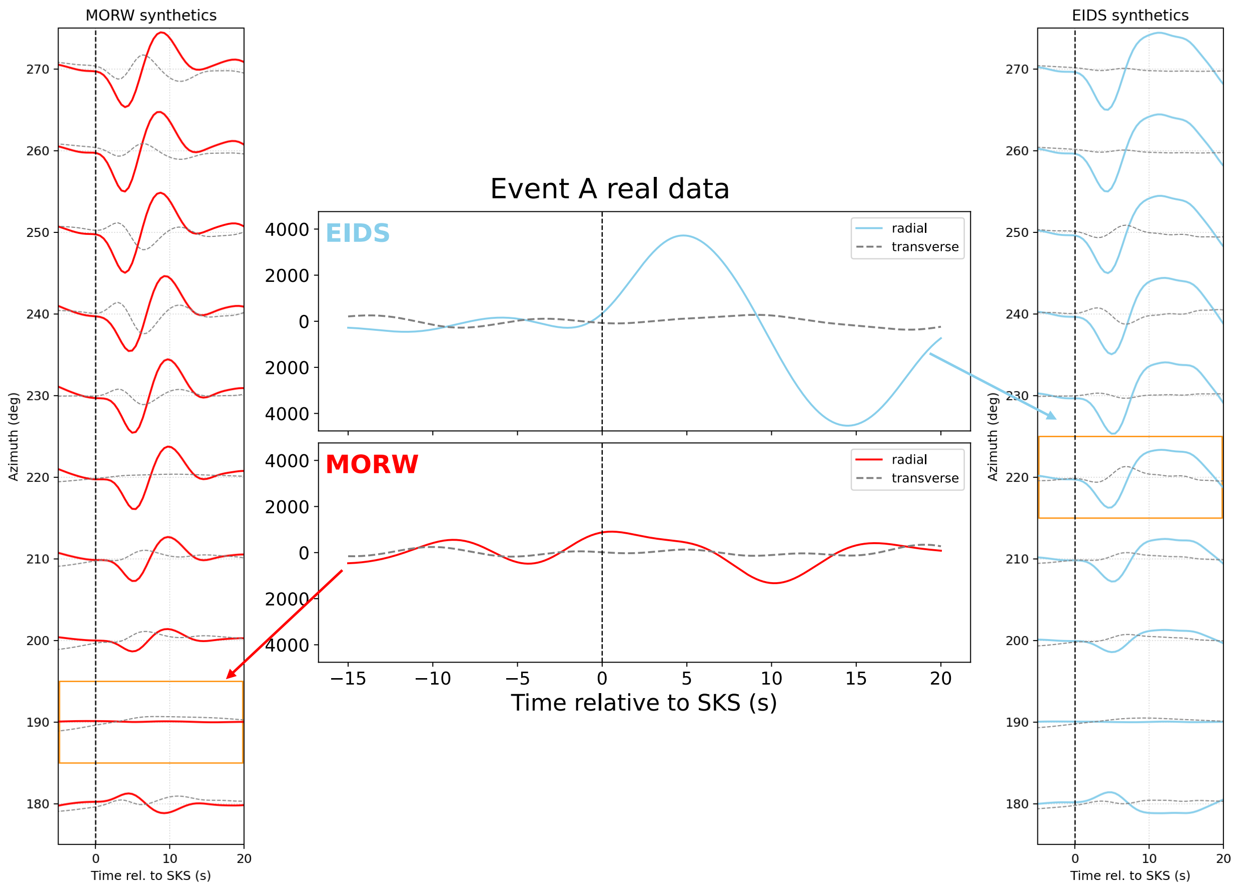

Figure 9. Central panel: comparison of the real SKS energy produced by event A at station EIDS in Queensland and MORW in WA. Coloured lines indicate the radial component of the seismometer (red for MORW, blue for EIDS), while the dashed grey lines are the transverse component. Dashed vertical black line is the predicted SKS arrival time from Earth model iasp91. Left panel: synthetics calculated for an event with the same focal mechanism as event A, but with varying azimuth from source to station, measured at station MORW. A synthetic splitting operator is applied to simulate the effect of seismic anisotropy on the isotropic Earth synthetics. The values of the splitting parameters are taken from Ba et al. (2023): $\phi = 47°$, δt = 1.46 s. The orange box indicates the azimuth of the real event to station MORW. Right panel: same as left, but for station EIDS. The splitting parameters taken from Ba et al. (2023) for station EIDS are $\phi = 49°$, δt = 0.99 s.

Alt text: Central panel compares real SKS energy produced by an event at station EIDS and station MORW. The outer panels plot synthetics calculated for an event with the same focal mechanism but varying azimuth from source to station, for stations MORW and EIDS.

the difference in SKS energy as the azimuth becomes coincident with the nodal plane strike (Figure 9). The synthetics are calculated using an isotropic Earth model (van Driel et al., 2015; Nissen-Meyer et al., 2014; Krischer et al., 2017). Therefore, to simulate the effect of seismic anisotropy, we add a synthetic splitting operator with parameters equal to those measured at station EIDS and station MORW by Ba et al. (2023). The splitting parameters are $\phi = 49°$, $\delta t = 0.99$ s for station EIDS and $\phi = 47°$, $\delta t = 1.46$ s for station MORW. These synthetics show that SKS energy is minimised at an azimuth of ~190°, which is close to the nodal plane strike for event A, 179°. Once the azimuth rotates away from this value, the SKS energy becomes more visible.

Even in this 'ideal' synthetic case with zero noise added, the XKS energy is so small as to be completely absent at an azimuth of ∼190°. Retrieving a shear-wave splitting measurement would therefore not be possible. When using real data, the presence of noise and the more complicated structure of the real Earth would mask the XKS signals further.

A typical signal-to-noise ratio (SNR) for filtering out poor XKS signals is 3: any events with equal or lower SNR than this are typically disregarded (e.g., Liu and Gao, 2013). In Figure 6, we plot the variation in maximum radial amplitude as the azimuth from an earthquake source to a receiver changes. A dashed grey line is plotted at one third of the peak-to-peak amplitude for the synthetics. This gives an indication of the azimuths that would likely be affected by the reduction in XKS energy close to the nodal plane. For a thrust fault, approximately 40% of azimuths lie below the line and are likely to be impacted, while for a strike-slip fault, ∼15% of azimuths lie below the line.

We conclude that the orientation of a focal mechanism relative to an event's source-to-receiver raypath can reduce the XKS energy substantially enough to influence the likelihood of recording an XKS measurement across a considerable range of azimuths (15–40%). Given the restricted back-azimuthal range of events typically available for XKS splitting, this can have a significant impact for particular regions of study, as we have outlined here for WA. Such factors should therefore be taken into consideration when interpreting the rate of return of results for shear-wave splitting studies globally.

Conclusion

Shear-wave splitting results for Phase 1 and 2 of the WA Array indicate that seismic anisotropy is pervasive across WA, with a predominant E–W to NE–SW fast polarisation orientation. However, the number of results at each station is low, with most stations only recording one or two splits over their year-long deployment. The lack of results is most striking when permanent stations are analysed: stations that have been operating for decades produce very few splits, as seen in multiple studies of anisotropy on the Australian continent. This has contributed to suggestions that the continent is apparently isotropic, or that anisotropy is very weak in the region.

After investigating the effect of the radiation pattern for various focal mechanisms on XKS energy, we conclude that the orientation of an event's nodal planes relative to the great circle path can adversely affect the ability to make shear-wave splitting measurements.

Due to the epicentral distance requirement for the XKS phases, earthquakes available for WA shear-wave splitting studies are predominantly located in the South American and Aleutian subduction zones. The focal mechanisms for these events are typically thrust or normal faults aligned parallel to the trench geometry. We find that the raypaths connecting these events to WA are often similarly aligned to the nodal planes. We show that this situation leads to a reduction in XKS energy, such that it is not feasible to make a measurement (either a split or a null).

Thus, a lack of measurements in a shear-wave splitting study does not necessarily indicate an absence of seismic anisotropy beneath the region. In WA, the similarity between the great circle path and the focal mechanism nodal planes from the main source regions (South America and the Aleutians) can explain the reduced number of measurements made, rather than the need to invoke apparent isotropy beneath the continent.

Our conclusions are useful for planning future proposed shear-wave splitting studies as well as interpreting limited results in other regions. We suggest that it is important to consider the plate boundaries that XKS events are predominantly sourced from and the typical orientation of these boundaries relative to the raypaths, in order to appropriately interpret the productivity of shear-wave splitting results.

Data and Resources

We used seismic data from the permanent AU and S1 networks (Geoscience Australia, 2021; Balfour et al., 2014; Salmon et al., 2011), and the temporary WA Array, OA and 1K networks (Gorbatov et al., 2020; Tkalčić et al., 2013; Geological Survey of Western Australia, 2022). The seismic data are all freely available via AusPass (http://auspass.edu.au/). The SplitLab software was utilized to calculate XKS splitting at these stations (Wüstefeld et al., 2008). Synthetics were computed using Instaseis and Syngine, based on AxiSEM (van Driel et al., 2015; Krischer et al., 2017; Nissen-Meyer et al., 2014). Figures and maps were plotted using Generic Mapping Tools (GMT) version 6 (Wessel et al., 2019) licensed under LGPL version 3 or later, available at https://www.genericmapping-tools.org. A full list of XKS splitting results for Phase 2 is available in Supplementary Data Set 1 and a full list of the XKS null results for Phase 2 is available in Supplementary Data Set 2. Supplementary Figures 1–3 are interactive plots of the SV and SH radiation for the standard double-couple focal mechanisms, calculated using the equations of Boore and Boatwright (1984). Figure 1 is a thrust fault, Figure 2 is a strike-slip fault and Figure 3 is a normal fault. A toggle in the upper left corner allows you to switch between the SV and SH patterns.

Declaration of Competing Interests

The authors acknowledge that there are no conflicts of interest recorded.[1]

Acknowledgments

The seismic data for Phase 2 of the WA Array were collected on the unceded sovereign Country of the Yamatji, Badima, Darlot, Nyalpa Pirniku, Kakarra, Ngadju, Marlinyu Ghoorlie and Esperance Nyungar peoples and nations. We thank them for their custodianship of the land and pay our respects to elders past, present and emerging.

We are grateful to colleagues at the Geological Survey of Western Australia for their hard work in planning and deploying the WA Array seismic network: Ruth Murdie, J.-P. O'Donnell, Huaiyu Yuan and others. Thank you to Robert Pickle and Reza Ebrahimi for their important work ensuring that the seismic data were of good quality.

References

Aki, K. and P. G. Richards (2002). *Quantitative seismology*.

Argus, D. F., R. G. Gordon, and C. DeMets (2011). Geologically current motion of 56 plates relative to the no-net-rotation reference frame. *Geochemistry, Geophysics, Geosystems* **12**(11).

[1] The authors acknowledge that there are no conflicts of interest recorded.

Ba, K., S. S. Gao, J. Song, and K. H. Liu (2023). Seismic azimuthal anisotropy beneath a fast moving ancient continent: Constraints from shear wave splitting analysis in Australia. *Journal of Geophysical Research: Solid Earth* **128**(2), e2022JB025866.

Balfour, N. J., M. Salmon, and M. Sambridge (2014). The Australian seismometers in schools network: Education, outreach, research, and monitoring. *Seismological Research Letters* **85**(5), 1063–1068.

Bird, P. (2003). An updated digital model of plate boundaries. *Geochemistry, Geophysics, Geosystems* **4**(3).

Birkey, A. and H. A. Ford (2023). Anisotropic structure of the Australian continent. *Frontiers in Earth Science* **10**, 1055480.

Boore, D. M. and J. Boatwright (1984). Average body-wave radiation coefficients. *Bulletin of the Seismological Society of America* **74**(5), 1615–1621.

Bowman, J. R. and M. Ando (1987). Shear-wave splitting in the upper-mantle wedge above the Tonga subduction zone. *Geophysical Journal International* **88**(1), 25–41.

Chen, X., V. Levin, and H. Yuan (2021). Small shear wave splitting delays suggest weak anisotropy in cratonic mantle lithosphere. *Geophysical Research Letters* **48**(16), e2021GL093861.

Dziewonski, A. M., T.-A. Chou, and J. H. Woodhouse (1981). Determination of earthquake source parameters from waveform data for studies of global and regional seismicity. *Journal of Geophysical Research: Solid Earth* **86**(B4), 2825–2852.

Eakin, C. M., D. R. Davies, S. Ghelichkhan, J. P. O'Donnell, and S. Agrawal (2023). The influence of lithospheric thickness variations beneath Australia on seismic anisotropy and mantle flow. *Geochemistry, Geophysics, Geosystems* **24**(9), e2023GC011066.

Eakin, C. M., C. Flashman, and S. Agrawal (2021). Seismic anisotropy beneath Central Australia: A record of ancient lithospheric deformation. *Tectonophysics* **820**, 229123.

Eakin, C. M. and M. D. Long (2013). Complex anisotropy beneath the Peruvian flat slab from frequency-dependent, multiple-phase shear wave splitting analysis. *Journal of Geophysical Research: Solid Earth* **118**(9), 4794–4813.

Eakin, C. M., M. Obrebski, R. M. Allen, D. C. Boyarko, M. R. Brudzinski, and R. Porritt (2010). Seismic anisotropy beneath Cascadia and the Mendocino triple junction: Interaction of the subducting slab with mantle flow. *Earth and Planetary Science Letters* **297**(3-4), 627–632.

Ebrahimi, R. (2026). Data Quality Assurance/Quality Control from Phase 2 of the WA Array Passive Seismic Project, Western Australia. In R. E. Murdie (Ed.), *WA Array Phase 2: Geological Survey of Western Australia*. In press.

Ekström, G., M. Nettles, and A. M. Dziewoński (2012). The global cmt project 2004–2010: Centroid-moment tensors for 13,017 earthquakes. *Physics of the Earth and Planetary Interiors* **200**, 1–9.

Fouch, M. J. and S. Rondenay (2006). Seismic anisotropy beneath stable continental interiors. *Physics of the Earth and Planetary Interiors* **158**(2-4), 292–320.

Gauntlett, M. and C. M. Eakin (2026). Shear-wave splitting across Phase 2 of the WA Array. In R. E. Murdie (Ed.), *WA Array Phase 2: Geological Survey of Western Australia*. In press.

Gauntlett, M., C. M. Eakin, N. Bishoyi, P. Zhang, J.-P. O'Donnell, R. E. Murdie, M. S. Miller, R. Pickle, and R. Ebrahimi (2025). Seismic anisotropy analysis across Southwestern Australia reveals ENE-trending lithospheric architecture linked to Archean Yilgarn Craton formation. *Geochemistry, Geophysics, Geosystems* **26**(12), e2025GC012589.

Geological Survey of Western Australia (2022). WA Array.

Geoscience Australia (2021). Australian National Seismograph Network Data Collection.

Gorbatov, A., K. Czarnota, B. Hejrani, M. Haynes, R. Hassan, A. Medlin, J. Zhao, F. Zhang, M. Salmon, H. Tkalčić, H. Yuan, M. Dentith, N. Rawlinson, A. M. Reading, B. L. N. Kennett, C. Bugden, and M. Costello (2020). AusArray: quality passive seismic data to underpin updatable national velocity models of the lithosphere. Geoscience Australia.

Gripp, A. E. and R. G. Gordon (2002). Young tracks of hotspots and current plate velocities. *Geophysical Journal International* **150**(2), 321–361.

Heintz, M. and B. L. Kennett (2005). Continental scale shear wave splitting analysis: Investigation of seismic anisotropy underneath the Australian continent. *Earth and Planetary Science Letters* **236**(1-2), 106–119.

Heintz, M. and B. L. Kennett (2006). The apparently isotropic Australian upper mantle. *Geophysical Research Letters* **33**(15).

Kendall, J.-M. and P. G. Silver (1996). Constraints from seismic anisotropy on the nature of the lowermost mantle. *Nature* **381**(6581), 409–412.

Krischer, L., A. R. Hutko, M. van Driel, S. Stähler, M. Bahavar, C. Trabant, and T. Nissen-Meyer (2017). On-demand custom broadband synthetic seismograms. *Seismological Research Letters* **88**(4), 1127–1140.

Liu, K. H., A. Elsheikh, A. Lemnifi, U. Purevsuren, M. Ray, H. Refayee, B. B. Yang, Y. Yu, and S. S. Gao (2014). A uniform database of teleseismic shear wave splitting measurements for the western and central United States. *Geochemistry, Geophysics, Geosystems* **15**(5), 2075–2085.

Liu, K. H. and S. S. Gao (2013). Making reliable shear-wave splitting measurements. *Bulletin of the Seismological Society of America* **103**(5), 2680–2693.

Long, M. D. and T. W. Becker (2010). Mantle dynamics and seismic anisotropy. *Earth and Planetary Science Letters* **297**(3-4), 341–354.

Martin, D. M., R. Murdie, H. Cutten, D. Kelsey, C. Thomas, R. Q. de Gromard, Y. Zhan, and P. Haines (2021). 1: 2 500 000 major crustal boundaries of Western Australia. *Accelerated Geoscience Program extended abstracts compiled by Geological Survey of Western Australia: Geological Survey of Western Australia Record* **4**, 20–22.

Miller, M. S., R. Pickle, R. Murdie, H. Yuan, T. I. Allen, K. Gessner, B. L. Kennett, and J. Whitney (2023). Southwest Australia Seismic Network (SWAN): recording earthquakes in Australia's most active seismic zone. *Seismological Society of America* **94**(2A), 999–1011.

Murdie, R. E., H. Yuan, J. P. O'Donnell, S. P. Johnson, R. Ebrahimi, and M. Rashidifard (2024). WA Array: A High-Resolution Passive-Source Seismic Survey to Image the West Australian Lithosphere. *Seismological Research Letters* **95**(5), 3093–3108.

Nicolas, A. and N. I. Christensen (1987). Formation of anisotropy in upper mantle peridotites: A review. *Composition, structure and dynamics of the lithosphere-asthenosphere system* **16**, 111–123.

Nissen-Meyer, T., M. van Driel, S. C. Stähler, K. Hosseini, S. Hempel, L. Auer, A. Colombi, and A. Fournier (2014). AxiSEM: broadband 3-D seismic wavefields in axisymmetric media. *Solid Earth* **5**(1), 425–445.

Özalaybey, S. and W.-P. Chen (1999). Frequency-dependent analysis of SKS/SKKS waveforms observed in Australia: evidence for null birefringence. *Physics of the Earth and Planetary Interiors* **114**(3-4), 197–210.

Salmon, M., N. Balfour, and M. Sambridge (2011). Australian Seismometers in Schools.

Savage, M. (1999). Seismic anisotropy and mantle deformation: what have we learned from shear wave splitting? *Reviews of Geophysics* **37**(1), 65–106.

Tkalčić, H., B. Kennett, C. Sippl, C. Spaggiari, and K. Gessner (2013). Albany-Fraser Experiment.

van Driel, M., L. Krischer, S. C. Stähler, K. Hosseini, and T. Nissen-Meyer (2015). Instaseis: instant global seismograms based on a broadband waveform database. *Solid Earth* **6**(2), 701–717.

Vinnik, L., L. Makeyeva, A. Milev, and A. Y. Usenko (1992). Global patterns of azimuthal anisotropy and deformations in the continental mantle. *Geophysical Journal International* **111**(3), 433–447.

Wüstefeld, A., G. Bokelmann, C. Zaroli, and G. Barruol (2008). SplitLab: A shear-wave splitting environment in Matlab. *Computers & Geosciences* **34**(5), 515–528.

Manuscript Received 00 Month 0000